

PAPER • OPEN ACCESS

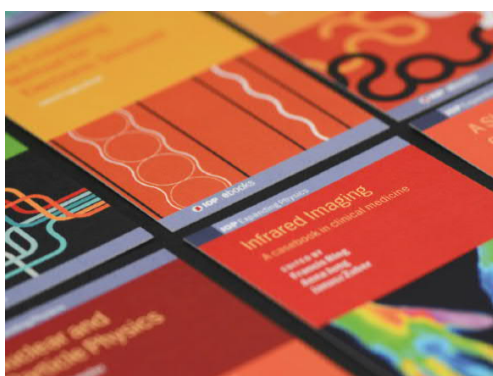
MEAM interatomic potentials of Ni, Re, and Ni–Re alloys for atomistic fracture simulations

To cite this article: Masud Alam *et al* 2022 *Modelling Simul. Mater. Sci. Eng.* **30** 015002

View the [article online](#) for updates and enhancements.

You may also like

- [Molecular dynamics simulations of dopant effects on lattice trapping of cracks in Ni matrix](#)
Shulan Liu, , Huijing Yang et al.
- [What defines the quantum regime of the free-electron laser?](#)
Peter Kling, Enno Giese, Rainer Endrich et al.
- [Construction and application of multi-element EAM potential \(Ni–Al–Re\) in / Ni-based single crystal superalloys](#)
J P Du, C Y Wang and T Yu



IOP | ebooks™

Bringing together innovative digital publishing with leading authors from the global scientific community.

Start exploring the collection—download the first chapter of every title for free.

MEAM interatomic potentials of Ni, Re, and Ni–Re alloys for atomistic fracture simulations

Masud Alam^{1,*} , Liverios Lymperakis¹ ,
Sébastien Groh²  and Jörg Neugebauer¹

¹ Department of Computational Material Design, Max-Planck-Institut für Eisenforschung GmbH, Max-Planck Str. 1, D-40237 Düsseldorf, Germany

² Theoretical Applied Physics-Computational Physics, Albert-Ludwigs-Universität Freiburg, Hermann-Herder-Str. 3, 79104 Freiburg, Germany

E-mail: masud.alam@ruhr-uni-bochum.de

Received 23 August 2021, revised 13 October 2021

Accepted for publication 15 November 2021

Published 2 December 2021



Abstract

Second nearest neighbor modified embedded atom method (2NN-MEAM) interatomic potentials are developed for the Ni, Re, and Ni–Re binaries. To construct the potentials, density functional theory (DFT) calculations have been employed to calculate fundamental physical properties that play a dominant role in fracture. The potentials are validated to accurately reproduce material properties that correlate with material's fracture behavior. The thus constructed potentials were applied to perform large scale simulations of mode I fracture in Ni and Ni–Re binaries with low Re content. Substitutional Re did not alter the ductile nature of crack propagation, though it resulted in a monotonous increase of the critical stress intensity factor with Re content.

Keywords: MEAM potential, brittle fracture, ductile fracture, Griffith theory, Rice theory, cohesive zone modeling

(Some figures may appear in colour only in the online journal)

1. Introduction

Ni based superalloys, also known as γ/γ' alloys, are characterized by high ductility, improved creep and fatigue resistance, as well as high melting temperature. Hence they constitute an

* Author to whom any correspondence should be addressed.



Original content from this work may be used under the terms of the [Creative Commons Attribution 4.0 licence](https://creativecommons.org/licenses/by/4.0/). Any further distribution of this work must maintain attribution to the author(s) and the title of the work, journal citation and DOI.

indispensable material system for high temperature gas turbine applications [1, 2]. Creep and fatigue properties of second and third generation Ni based super alloys could be significantly improved by the addition of 3 wt% and 6 wt% Re [3–5]. However, the mechanisms governing this so-called *rhenium effect* are still under debate (see reference [6] and references therein). Possible mechanisms include the formation of $D_{1\alpha}$ phases which retard the dislocation climb [7], hinder or delay the coarsening of the γ' phase due to the low Re diffusion constant.

Several phenomena occur at a crack tip during fracture. These span different length scales [8–10] and range from bond breaking to lattice trapping in the scale of a few Å to long range elastic strain fields in the sub- μm scale. Therefore, a full on-atomic-scale description of fracture requires simulation cells consisting of at least a few ten thousand atoms [11]. Although density functional theory (DFT) calculations are capable to accurately describe both the atomistic scale mechanisms as well as the long range elastic fields, their computational cost still restricts them to system sizes containing a few thousand atoms. A widely used methodology applied in atomic-scale fracture studies is to employ semi-empirical interaction models such as the embedded atom method (EAM) or the modified embedded atom method (MEAM) potentials [12, 13]. These approaches allow to treat system sizes of a few million atoms.

For Ni, there is a large number of interatomic potentials reported in the literature [14–17]. Among others, Lee *et al* [14] developed a Ni interatomic potential in the 2NN MEAM framework to describe the physical properties of Ni. Ko *et al* [15] developed a Ni potential to describe martensitic phase transitions in Ni–Ti. Similarly, interatomic potentials were developed in both the EAM and MEAM framework for Re [18, 19]. The EAM potentials of Re developed by Bonny *et al* [18] were trained to predict the properties of the W-Re solid solution whereas MEAM Re potentials were fitted to reproduce only selected physical properties such as elastic constants, vacancy formation energy, and cohesive energy difference between hcp to bcc phase [19].

We tested a large number of existing Ni and Re interatomic potentials to benchmark their ability to model fracture behavior. Specifically, these potentials were tested against physical properties known to correlate with the fracture behavior, e.g. surface energies, stacking fault energies, elastic constants, as well as work of separation and traction separation behavior. In figure 1 the calculated tensile stress employing the above mentioned potentials is plotted against the separation displacement for the Ni {112} cleavage plane. All potentials that were tested show either discontinuous traction separation or unrealistically negative traction separation. These potentials' artifacts qualitatively affect crack propagation and show, e.g. unrealistic crack tip blunting in atomistic simulations [12, 20].

In the present work we parametrize a second nearest neighbor (2NN) MEAM interatomic potential for Ni, Re, and Ni–Re binary system. These potentials are trained using an extensive set of materials properties that are collected in a materials' database. This database includes elastic constants, surface energies, generalized stacking fault energy surfaces, work of separations and structural transition energies. The performance of these potentials is further evaluated by calculating the critical stress intensity factor from direct atomistic simulations, and comparing it to those calculated from Griffith theory [21] and Rice dislocation emission criteria [22].

Employing these potentials, we investigate and compare the mode I fracture behavior of Ni with and without Re solute e.g. the opening mode by the application of a tensile load perpendicular to the crack plane. We consider different crack orientations, and our calculations reveal that the critical stress intensity factor derived from continuum based theory, i.e. linear elastic fracture mechanics (LEFM), are within 10%–20% to DFT calculated values. Moreover, we find that with increasing Re concentrations in Ni, the critical stress intensity factor increases.

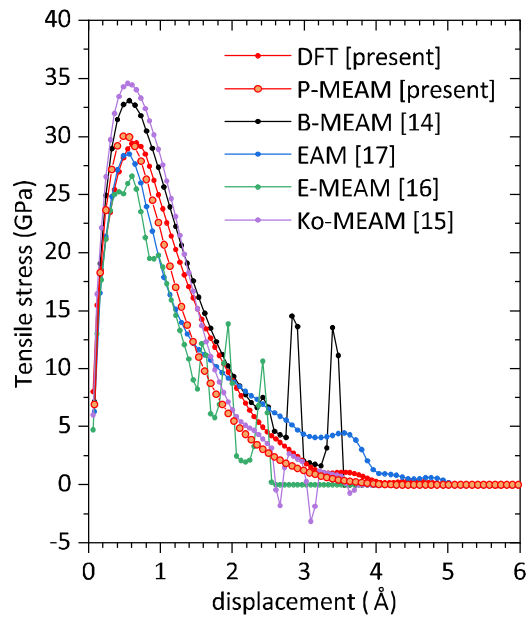


Figure 1. Comparison of tensile stress of Ni {112} as function of the separation displacement among different interatomic potentials and DFT. Ko-MEAM, EAM, B-MEAM and E-MEAM refers to the potentials 15, 17, 14 and 16 respectively. P-MEAM is the potential fitted in the present work.

Such increase in critical stress intensity factor of Ni due to the addition of Re is in line with the enhanced ductility of Ni due to the addition of Re.

The main objective of the paper is to parametrize and evaluate 2NN-MEAM potentials suitable to study fracture in Ni and Ni–Re alloys. The workflow to achieve this is schematically shown in figure 2. The paper is organized as follows: in section 2 a brief description of the fundamentals of linear elastic fracture mechanics (LEFM) of an elastically isotropic medium is given. Furthermore, the physical parameters that govern fracture are provided. The parametrization of the potentials is discussed in section 3 together with the details of the DFT calculations employed to derive the data for the materials' database. In the same section the calculated material properties that correlate with LEFM and fracture, e.g. the generalized stacking fault energies (GSFE), the surface energies, the surface traction-separation and the works of separation are presented. Moreover, the predicted melting temperatures are also provided. In section 4 the atomistic simulations of fracture at a crack tip in Ni and Ni–Re are presented and discussed in comparison to the predictions of LEFM. In section 5 we summarize our results.

2. Linear elastic fracture mechanics

The ductile and brittle failure of a material is characterized by the mechanisms occurring at the crack tip: while dislocation emission is a signature of ductile fracture, bond cleavage is the underlying mechanism of brittle fracture. The critical stress intensity factor, K_{Rice} , for a dislocation to nucleate at a crack tip in mode I fracture was proposed by Rice [22]. Within

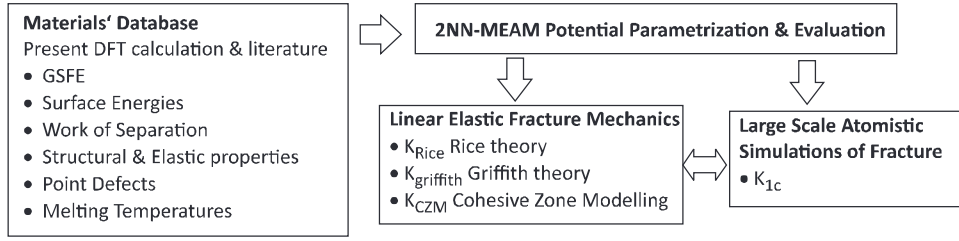


Figure 2. Schematic representation of the workflow to parametrize, evaluate, and apply the 2NN-MEAM potentials to investigate fracture in Ni and Ni-Re alloys. The construction of the materials' database and the parametrization of the potential are provided in section 3. The LEFM is discussed in section 2 and the large scale atomistic simulations in section 4.

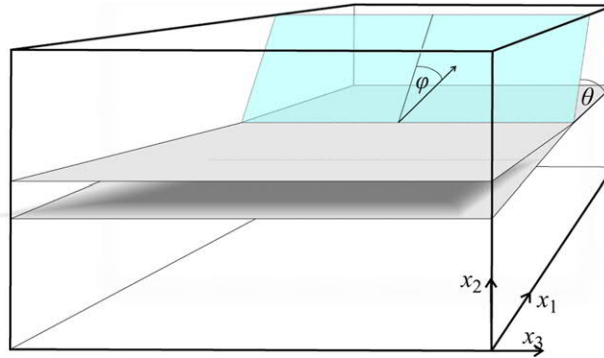


Figure 3. Schematic representation of the crack geometry used to compute K_{Rice} . θ is the angle between slip plane and crack plane and ϕ is the angle between the crack front normal and the Burgers vector. The inclined plane indicates the slip plane and the arrow indicates the Burgers vector.

isotropic elasticity, K_{Rice} is defined as

$$K_{\text{Rice}} = \cos^2(\theta/2) \sin(\theta/2) \sqrt{\frac{2\mu}{1-\nu} \gamma_{\text{us}} (1 + (1-\nu)\tan^2 \phi)}, \quad (1)$$

where μ and ν are the shear modulus and the Poisson ratio, respectively. θ and ϕ denote the angle between the slip plane and crack plane and the angle between the crack front normal and the Burgers vector, respectively (see figure 3). γ_{us} is the unstable stacking fault energy which is obtained from the generalized stacking fault energy (GSFE) curve [23].

As already mentioned, the brittle fracture of a material is determined by bond cleavage. Once the surfaces energies and elastic properties are known, the critical stress intensity factor can be evaluated using Griffith theory. Within Griffith theory and plane strain conditions, the critical stress intensity factor, K_{Griffith} , for mode I brittle fracture is defined as

$$K_{\text{Griffith}} = \sqrt{\frac{2E\gamma}{1-\nu^2}}, \quad (2)$$

where γ is the surface energy, and E is the Young modulus.

In addition to Griffith criterion, we have also considered the cohesive zone modeling (CZM), which is known to control the path transformation of brittle fracture. This model is extensively used in predicting crack growth behavior both at the mesoscale [24, 25] as well as at the atomistic scale [12, 26]. Within CZM and for an isotropic homogeneous solid, the critical stress intensity factor, K_{CZM} , is defined as

$$K_{CZM} = \sqrt{\frac{E w}{1 - \nu^2}}, \quad (3)$$

where w is the work of separation.

The aforementioned discussion and equations (1)–(3) indicate that a prerequisite to investigate fracture in Ni and Ni–Re crystals by large scale atomistic calculations is the availability of an interatomic potential that is able to accurately describe surfaces energies, GSFE, and traction separation curves. Additional properties included in the Ni, Re, and Ni–Re materials’ database are the cohesive energy, the heat of formation for the ground state crystal structure as well as for higher energy structures, lattice and elastic constants, work of separation for low index surfaces, and vacancy formation energies.

3. Methodology

3.1. *Ab-initio calculations*

In order to build the aforementioned materials’ database we employ spin polarized density functional theory (DFT) calculations. The calculations are performed using the Vienna *ab-initio* simulation package, VASP [27]. For the bulk calculations, a kinetic energy cutoff of 400 eV is used for the expansion of the plane wave basis set along with $6 \times 6 \times 6k$ -points for the Brillouin zone integration. The generalized gradient approximation (GGA-PBE) is used. Interactions between core and valence electrons are described by PAW PBE pseudopotentials with ten and seven valence electrons for Ni and Re, respectively. For the calculation of the surface energies, we employ a slab geometry with more than ten unit cells along the direction normal to the surface with at least 40 atoms in the supercell. A vacuum of 10 Å is included in the repeated slab geometry. The atoms are relaxed using the conjugate gradient relaxation algorithm until the forces on each atom are smaller than 0.01 eV Å⁻¹. Similar geometries are adopted for the calculation of the GSFE. The methodology for the calculations of the elastic constants, the GSFE, the surface energies, and the traction separation stress are adopted from previous works [12, 23, 28–30].

3.2. *2NN MEAM potential parametrization*

In the 2NN MEAM potential formalism, there are sixteen parameters for the unary system (see table 1) and thirteen additional parameters for the binary system (see table 2). The potential’s formalism is given in the appendix. The methodology for fitting the parameters follows our earlier works [12, 28, 31].

For the unary Ni and Re systems, the cohesive energy, E_c , and the equilibrium nearest neighbor distances, r_c , are obtained from existing MEAM potentials [14, 18] considering the fcc and hcp crystal structures, respectively. The parameter α is proportional to the square root of the bulk modulus, B . Combinations of the four decay lengths of the partial electron densities ($\beta_h : h = 0-3$) and the three scaling factors of the background electron density ($t_h : h = 1-3$) are used to fit the surface energies, the elastic constants, the GSFE, and the tensile stress curves. Parameter A is a scaling factor of the embedding function energy. This is used in combination

Table 1. 2NN MEAM potential parameter sets for Ni and Re. The units of E_c are eV and of r_e , r_c , and Δr are Å. The reference structures for Ni and Re are fcc and hcp, respectively.

E_c	r_e	β_0	β_1	β_2	β_3	α	A	C_{\min}	t_1	t_2	t_3	C_{\max}	r_c	Δr	δ
Ni	4.45	2.76	3.107	2.4	1.5	4.0	5.308	1.0	0.7	1.8	1.36	2.85	5.5	2.0	0.05
Re	8.03	2.49	4.5	2.40	7.285	4.0205	6.2402	0.74	5.60	3.5	-4.02	2.85	10.80	0.4	0.01

Table 2. 2NN MEAM potential parameters set for Ni–Re binary. The units of the cohesive energy $E_c(\text{Ni, Re})$ and the first nearest neighbors, cutoff and smoothing distances are in eV and Å, respectively. The reference structure for NiRe is B2(CsCl).

Parameters	Values	Parameters	Values
$E_c(\text{Ni, Re})$	6.165	$C_{\min}(\text{Ni, Ni, Re})$	2.10
$r_e(\text{Ni, Re})$	2.555	$C_{\max}(\text{Ni, Re, Re})$	2.85
$\alpha(\text{Ni, Re})$	5.85	$C_{\min}(\text{Ni, Re, Ni})$	0.70
Δr	2.0	$C_{\min}(\text{Ni, Re, Re})$	1.90
r_c	5.5	$C_{\min}(\text{Re, Re, Ni})$	1.90
$C_{\max}(\text{Ni, Re, Ni})$	3.0	$C_{\max}(\text{Re, Re, Ni})$	2.7
$C_{\max}(\text{Ni, Ni, Re})$	4.3		

with the parameter β_0 to correlate the cohesive energy differences between fcc and bcc Ni, and hcp and fcc Re. Two parameters, C_{\min} and C_{\max} , control the screening of the many body interactions and are used to fit the GSFE. The cutoff distance, r_c , the soothing distance, Δr , and the parameter δ are fit such that the interaction between two cleaved surfaces decays smoothly to zero at large separation distances.

To fit the parameters for the Ni–Re interactions we consider the CsCl structure as a reference structure. $E_c(\text{Ni, Re})$, $\alpha(\text{Ni, Re})$, $r_e(\text{Ni, Re})$ are fit to the DFT calculated cohesive energy, nearest neighbor distance, and bulk modulus of NiRe in the reference structure, respectively. The radial cutoff distance and the smoothing distance for the radial cutoff are set to 5.5 Å and 2.0 Å, respectively. The remaining eight parameters ($C_{\min}(M_i, M_j, M_k)$ and $C_{\max}(M_i, M_j, M_k)$, where $M_{i,j,k}$ denote Ni and/or Re) control the screening of the many body Ni–Re interactions. They are used to fit the elastic constants of the CsCl structure and the substitutional and interstitial formation energies of Re solute in Ni.

3.2.1. Generalized stacking fault energies. The GSFE profiles of Ni are calculated for shear along $\langle 110 \rangle$ and $\langle 112 \rangle$ in the $\{111\}$ glide plane (see figures 4(a) and (b), respectively). In these figures, we also plot the GSFE profiles obtained from DFT, previous EAM [17] and MEAM [14] (B-MEAM) potentials. The DFT calculated GSFE profile for shear along $\langle 110 \rangle$ is included in the material’s database. The unstable stacking fault energy (USFE) is obtained at the reduced displacement $u/b = 0.5$, where b is the norm of the Burgers vector and u is the displacement. The present MEAM (P-MEAM) potential underestimates the USFE with respect to the DFT calculated value, e.g. 47.93 vs 60.2 meV Å⁻². Nevertheless, such discrepancy is not critical: perfect dislocations from $\langle 110 \rangle \{111\}$ are expected to dissociate in two partials with Burgers vectors in the $\langle 112 \rangle$ direction. The GSFE profile for shear along $\langle 112 \rangle$ in the $\{111\}$ plane is plotted in figure 4(b). The P-MEAM potential agrees qualitatively with the DFT calculated GSFE profile. Quantitatively, the P-MEAM calculated stable and unstable stacking fault energies are 2.74 and 24.38 meV Å⁻², respectively while the corresponding DFT calculated values are 9.3 and 16.8 meV Å⁻², respectively.

The P-MEAM calculated GSFE profiles of hcp Re for shear along $\langle \bar{1}2\bar{1}0 \rangle$ in the basal plane and along $\langle \bar{1}2\bar{1}0 \rangle$ in the $\{10\bar{1}0\}$ plane are plotted against DFT and EAM [18] calculations in figures 5(a) and (b), respectively. The former is included in the material’s database. For the $\langle \bar{1}2\bar{1}0 \rangle \{0001\}$ slip system the P-MEAM calculated values of unstable and stable fault energies are 41.28 and 8.31 meV Å⁻², respectively. The corresponding DFT calculated values are 42.0 and 15.08 meV Å⁻², respectively. In the $\langle \bar{1}2\bar{1}0 \rangle \{10\bar{1}0\}$ slip system there is no stable stacking fault. The USFE is 83.62 meV Å⁻² which is in good agreement with the DFT calculated value of 68.69 meV Å⁻².

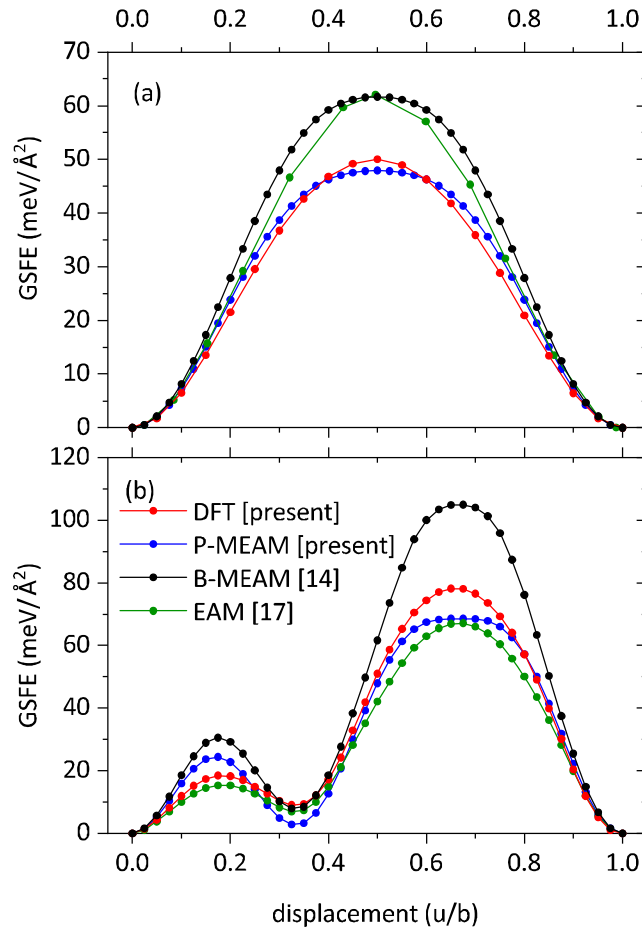


Figure 4. GSFE profiles for Ni as function of crystal displacements along (a) $\langle \bar{1}10 \rangle$ and (b) $\langle \bar{1}\bar{1}2 \rangle$ shear directions in the $\{111\}$ plane obtained from DFT, P-MEAM potentials, as well as EAM [17] and B-MEAM [14] potentials.

3.2.2. Surface energies. As can be seen from equation (2), a necessary prerequisite for an interatomic potential to describe brittle/ductile phenomena is the accurate description of the surface energies. Therefore, we calculate the surface energies of low index Ni and Re surfaces that may bound a crack. For fcc Ni, we consider the low index (100), (110), (111), and (112) surfaces. For Re, the basal plane (0001) as well as the $(1\bar{1}00)$ and $(11\bar{2}0)$ surfaces are considered. The DFT calculated surface energies of the (100), (110) surfaces of Ni, and (0001) surface of hcp Re are used to fit the potential. In order to calculate the surface energies we employ slab geometries consisting of 10 unit cells along the surface normal and 1×1 surface unit cells. The slabs are bound by two symmetry equivalent surfaces and a vacuum region of 10 Å. The atoms within the top and bottom 4 units are allowed to fully relax while the other atoms are kept fixed at their bulk-like positions. The surface energy, E_{surf} , is defined as

$$E_{\text{surf}} = \frac{1}{2A} (E_{\text{slab}} - nE_{\text{bulk}}), \quad (4)$$

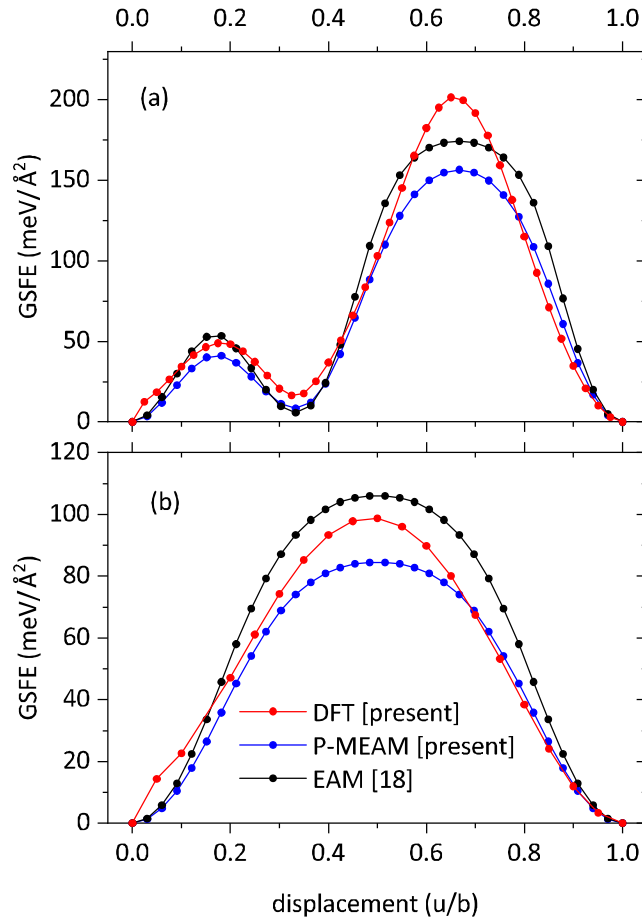


Figure 5. GSFE profiles for Re as function of crystal displacements along (a) the $\langle \bar{1}2\bar{1}0 \rangle$ shear direction in the basal plane and (b) the $\langle \bar{1}2\bar{1}0 \rangle$ shear direction in the $\{10\bar{1}0\}$ plane obtained from present 2NN MEAM, DFT and EAM [18] potential calculations.

where E_{slab} is the total energy of the slab consisting of n atoms, and E_{bulk} is the total energy per atom of bulk. A is the surface area and the factor 2 in the denominator accounts for the two symmetry equivalent surfaces in the slab geometry.

The calculated energies of Ni and Re surfaces are listed in tables 3 and 4, respectively. P-MEAM underestimates and overestimates the Ni and Re surface energies, respectively, with respect to DFT. Nevertheless, there is an overall agreement between P-MEAM and DFT within $18 \text{ meV } \text{\AA}^{-2}$ and $30 \text{ meV } \text{\AA}^{-2}$ for Ni and Re, respectively. Moreover, P-MEAM provides an excellent qualitative agreement with DFT: the energy differences to the energetically most favorable surface, i.e. the (111)Ni and (0001)Re, is within $14 \text{ meV } \text{\AA}^{-2}$ and $30 \text{ meV } \text{\AA}^{-2}$ in agreement to DFT.

3.2.3. Work of separation. In order to calculate the work of separation we perform a series of uniaxial tensile tests along the $\langle 100 \rangle$, $\langle 110 \rangle$, $\langle 111 \rangle$, and $\langle 112 \rangle$ directions of fcc Ni, and along the $\langle 0001 \rangle$, $\langle 1\bar{1}00 \rangle$, and $\langle 11\bar{2}0 \rangle$ directions of hcp Re. The work of separation of the (100) Ni and (0001) Re planes is included in the materials' database. The work for separating a surface

Table 3. Calculated physical properties of Ni using the present 2NN MEAM potential as well as previous the B-MEAM, EAM potentials and experimental data. All the properties are for fcc Ni unless it is otherwise denoted. The cohesive energy E_c of fcc Ni is in eV per atom, and ΔE are the differences in the cohesive energy in meV per atom of other Ni crystalline phases. a is the lattice constant in Å and c/a the ratio of lattice constants of the hcp structure. The unit of the bulk modulus is GPa. The units of the other properties are listed in the table. Properties with an asterisk [^(*)] have been included in the materials' database and employed to fit the potential. The superscript p (p) indicates present DFT calculations.

		P-MEAM	B-MEAM [14]	EAM [17]	DFT/experimental
fcc Ni	^(*) E_c	-4.45	-4.45	-4.45	-4.842 [15], -4.801 ^p
	^(*) a	3.521	3.521	3.52	3.524 [15], 3.52 ^p
	^(*) B	185	170	181	190.9 [15], 185 ^p
	B'	4.84	4.69	5.22	5.05 ^p
bcc	^(*) ΔE	160	160	112	93 [15], 97 ^p
	a	2.79	2.79	2.79	2.805 ^p
sc	ΔE	507	660	833	705 ^p
	a	2.32	2.35	2.35	2.33 ^p
hcp	ΔE	6.78	21	21	26 [15], 24 ^p
	a	2.49	2.49	2.48	2.488 ^p
	c/a	1.63	1.63	1.63	1.645 ^p
	Elastic constant (GPa)	^(*) C_{11}	290	260	247
	^(*) C_{12}	161	150	148	155 [15], 155 ^p
	^(*) C_{44}	101	131	125	129 [15], 132 ^p
Vacancy formation energy (eV)	E_v	1.18	1.97	1.6	1.41 [15], 1.42 ^p
	^(*) $\gamma_{(100)}$	130	178	117	151 [32], 135 ^p
	^(*) $\gamma_{(110)}$	129	176	128	148 [32], 147 ^p
	$\gamma_{(111)}$	106	148	101	125 [32], 120 ^p
Surface energy (meV Å ⁻²)	$\gamma_{(112)}$	124	171	122	142 ^p , 140 ^p
Cohesive strength (GPa)	$\sigma_{(100)}$	32	35	28	29 ^p
	$\sigma_{(110)}$	29	32	29	29 ^p
	$\sigma_{(111)}$	29	33	28	29 ^p
	$\sigma_{(112)}$	30	33	28	28 ^p
Critical opening displacement (Å)	$\delta_{(100)}$	0.56	0.57	0.56	0.5 ^p
	$\delta_{(110)}$	0.48	0.57	0.56	0.6 ^p
	$\delta_{(111)}$	0.48	0.48	0.48	0.45 ^p
	$\delta_{(112)}$	0.48	0.56	0.56	0.55 ^p
Work of separation (meV Å ⁻²)	^(*) $w_{(100)}$	254	346	270	253 ^p
	$w_{(110)}$	253	341	286	279 ^p
	$w_{(111)}$	210	290	250	230 ^p
	$w_{(112)}$	246	335	282	267 ^p
Melting temperature (K)	T_{Ni}	1550	2013	1635	1455 [33]

to infinite distance is calculated as following: at first, a simulation box consisting of 10 units normal to the surface of interest and a 1×1 unit cell in the cleavage plane is constructed. The cell is then divided into two parts across the cleavage plane. The distance between them is incrementally increased with a step size of 0.08 Å. The tensile stress, σ , is then calculated by the first derivative of the total energy, E , with respect to the applied strain, ε , using the following equation

$$\sigma = \frac{1}{V(\varepsilon)} \frac{dE}{d\varepsilon}, \quad (5)$$

Table 4. Calculated physical properties of Re using the present 2NN MEAM potential as well as the previous EAM potential and experimental data or DFT data. All the properties are for hcp Re unless it is otherwise stated. The units are as in table 3. The superscript p (p) indicates present DFT calculations.

		P-MEAM	EAM [18]	DFT/experimental
hcp Re	$^{(*)}E_c$	−8.03	−8.03	−7.82 ^p , −8.03 [34]
	$^{(*)}a$	2.765	2.761	2.77 ^p
	c/a	1.623	1.614	1.615 ^p
	$^{(*)}B$	373	382	303 ^p
	B'	5.21	3.08	19 ^p
fcc	$^{(*)}\Delta E$	27.26	20.0	63 ^p
	$^{(*)}a$	3.91	3.90	2.58 ^p
bcc	ΔE	200	130	315 ^p
	a	3.10	3.05	3.11 ^p
sc	ΔE	1617	1944	1365 ^p
	a	2.60	2.63	2.58 ^p
Elastic constant (GPa)	$^{(*)}C_{11}$	609	611	613 [35]
	$^{(*)}C_{12}$	286	299	270 [35]
	$^{(*)}C_{44}$	124	159	163 [35]
	$^{(*)}C_{33}$	705	682	683 [35]
	$^{(*)}C_{13}$	208	234	206 [35]
Vacancy (eV)	E_v	3.22	3.49	3.27 ^p
	$^{(*)}\gamma_{(0001)}$	188	140	158 ^p
Surface energy (meV \AA^{-2})	$\gamma_{(10\bar{1}0)}$	194	151	184 ^p
	$\gamma_{(\bar{1}2\bar{1}0)}$	213	183	192 ^p
	$\sigma_{(0001)}$	48.17	57.27	38 ^p
Cohesive strength (GPa)	$\sigma_{(10\bar{1}0)}$	47.31	59.19	40 ^p
	$\sigma_{(\bar{1}2\bar{1}0)}$	45.83	59.36	38 ^p
	$\delta_{(0001)}$	0.45	0.33	0.55 ^p
Critical opening displacement (\AA)	$\delta_{(10\bar{1}0)}$	0.47	0.34	0.5 ^p
	$\delta_{(\bar{1}2\bar{1}0)}$	0.53	0.39	0.6 ^p
	$^{(*)}w_{(0001)}$	367	318	333 ^p
Work of separation (meV \AA^{-2})	$w_{(10\bar{1}0)}$	377	344	361 ^p
	$w_{(\bar{1}2\bar{1}0)}$	407	397	387 ^p
	T_{Re}	4350	4836	3186 [33]

where $V(\varepsilon)$ is the volume at strain ε . The highest stress corresponds to the cohesive strength. The strain at the cohesive strength is the point where the crack starts to form and corresponds to the critical opening displacement or the characteristic length of fracture. The area enclosed under the stress–strain curve is the work of separation w .

In figure 6 the tensile stress as function of the separation displacement calculated by the P-MEAM potential for the above mentioned cleavage planes in fcc Ni is plotted. For comparison, stress–displacement profiles calculated by DFT as well as by B-MEAM and EAM interatomic potentials are also shown. The P-MEAM potential accurately reproduces the DFT stress vs displacement profiles both in the high tensile region as well as at the tail of the profile. The calculated cohesive strengths, critical opening displacements and work of separations are listed in table 3. The cohesive strengths show a weak dependence on the cleavage plane orientation: P-MEAM predicts cohesive strengths in the range of 29–32 GPa while DFT predictions are in the range of 28–29 GPa. The P-MEAM calculated works of separation and the critical opening displacements agree within 40 meV \AA^{-2} and 0.18 \AA , respectively, with the respective DFT results.

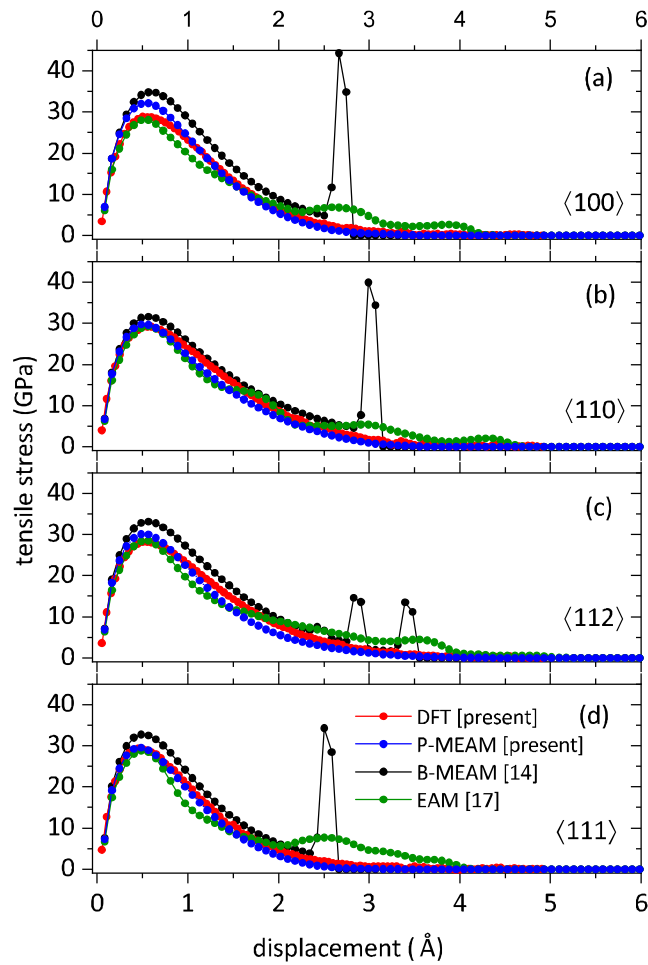


Figure 6. Tensile stress as function of the separation displacement along (a) $\langle 100 \rangle$, (b) $\langle 110 \rangle$, (c) $\langle 112 \rangle$, and (d) $\langle 111 \rangle$ calculated by the DFT, P-MEAM, B-MEAM [14] and EAM [17] potentials. The traction separation profile along $\langle 100 \rangle$ has been included in the materials' database. The other profiles are used to evaluate the P-MEAM potential.

A striking difference between P-MEAM, EAM and B-MEAM in the calculated stress–displacement profiles is the occurrence of spurious oscillations in the tail region of the latter potentials. The magnitude of these spurious oscillations is considerably large in the B-MEAM calculated profiles. For this potential, the oscillations are attributed to discontinuities in the energy vs displacement curves caused by the abrupt truncation of the pair potential at the cut-off distance. These oscillations constitute an artifact of the interatomic potential and have important consequences on the prediction of the brittle/ductile behavior by atomistic simulations. Indeed, Ko *et al* [20] showed that these oscillations induce an artificial energy barrier for brittle–ductile transitions and are also responsible for a spurious crack blunting in fracture simulations.

The tensile stress as function of the separation displacement for three Re planes is shown in figure 7 alongside DFT and EAM calculations. The calculated cohesive strengths, critical

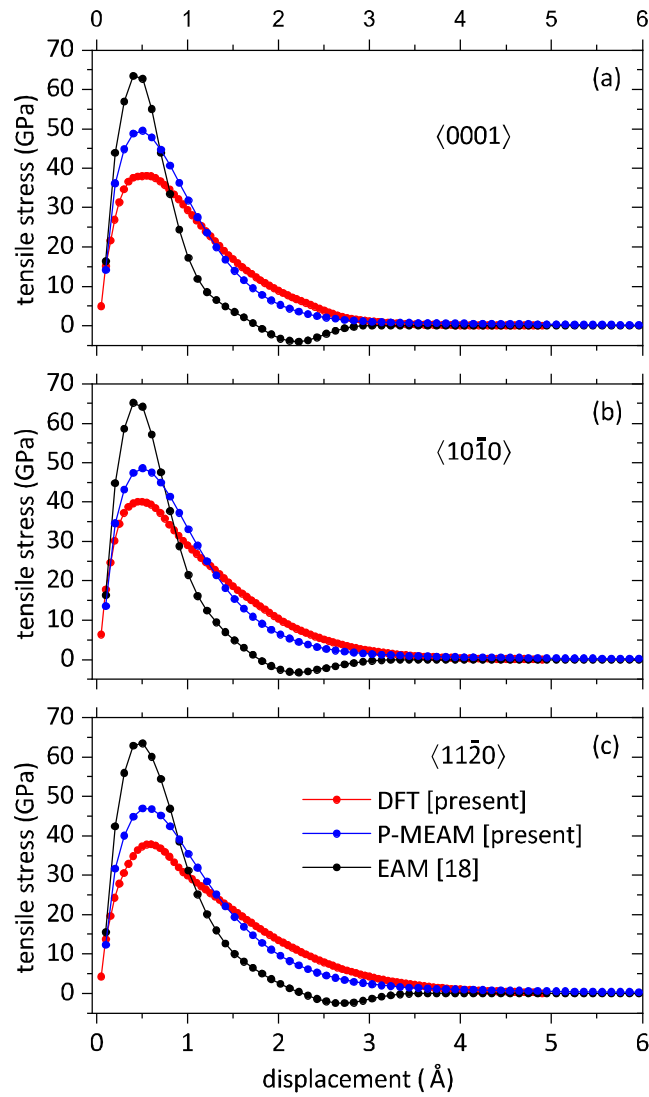


Figure 7. Tensile stress as function of the separation displacement along (a) $\langle 0001 \rangle$, (b) $\langle 10\bar{1}0 \rangle$, and (c) $\langle 11\bar{2}0 \rangle$ calculated by DFT, P-MEAM, and EAM [18] potentials. The traction separation profile along $\langle 0001 \rangle$ has been included in the materials' database. The other profiles are predictions.

opening displacements and work of separations are listed in table 4. The P-MEAM potential agrees qualitatively with the DFT data. The P-MEAM calculated cohesive strengths, critical opening displacements, and work of separations agree within 10.2 GPa, 0.08 Å, and 19 meV Å⁻², respectively, with DFT. On the other hand, the EAM potential shows artificial minima in the tensile stress within the displacements region of 2–3 Å. It also severely overestimates the critical strength, i.e. by 17 GPa or $\approx 42\%$, for the basal plane and even more for the $\langle 1\bar{1}00 \rangle$ and $\langle 11\bar{2}0 \rangle$ planes.

3.2.4. Structural and elastic properties. The elastic constants are computed by applying volume conserving strain deformations to the fcc Ni and hcp Re bulk unit cells [29]. They agree within 28 and 40 GPa with the experimental elastic constants for Ni and Re, respectively (see tables 3 and 4). We further evaluate the transferability of the P-MEAM potential by calculating the equilibrium lattice constants and the energy difference to fcc Ni and hcp Re for several metastable and unstable crystal phases. As can be seen in tables 3 and 4, apart from hcp Ni, they agree within less than 0.6 \AA^3 with the DFT calculated equilibrium volumes. P-MEAM as well as B-MEAM and EAM potentials underestimate the equilibrium volume of hcp Ni by more than 40% with respect to DFT. The cohesive energy differences of the aforementioned metastable crystal structures with the ground state fcc Ni and hcp Re structures are also in qualitative agreement with DFT.

To calculate the vacancy formation energies in fcc Ni and hcp Re we used $4 \times 4 \times 4$ bulk supercells. The vacancy formation energy, E_v , is defined as

$$E_v = E_{\text{tot}}^v(n) - n\mu_{\text{bulk}}, \quad (6)$$

where $E_{\text{tot}}^v(n)$ is the total energy of the supercell consisting of n atoms and a vacancy. μ_{bulk} is the chemical potential in the bulk phase. The P-MEAM calculated E_v of both Ni and Re are in excellent agreement to DFT, i.e. 1.18 vs 1.41 eV for Ni and 3.22 vs 3.27 eV for Re, respectively.

3.2.5. Properties of the Ni–Re binary. To fit the parameters that describe the Ni–Re interaction we consider the CsCl structure as reference structure. Further, we include in the materials' database the lattice as well as elastic constants, the cohesive and mixing enthalpy, and the formation energies of Re substitutional and interstitial defects in fcc Ni. To evaluate the performance of the potential we also calculate the lattice and elastic constants and heat of formation of Ni_4Re in the D1_a structure, which is the ground state at 20 at.% Re [7].

The substitutional, E_{sub}^f , and interstitial, E_{inter}^f , formation energies are written as

$$E_{\text{sub/inter}}^f = E_{\text{tot}}(n) - nE_{\text{tot}}^{\text{bulk}} - \mu_{\text{Re}}, \quad (7)$$

where $E_{\text{tot}}(n)$ is the total energy of the system consisting of n Ni atoms and an interstitial or substitutional Re. $E_{\text{tot}}^{\text{bulk}}$ is the total energy per atom of bulk fcc Ni, i.e. the chemical potential of Ni is fixed to the one of bulk fcc Ni. μ_{Re} is the chemical potential of Re and is fixed to that of Re in bulk hcp. The Re substitutionals binding energy E_{bind} is

$$E_{\text{bind}} = E_{2\text{sub}}^f - 2E_{\text{sub}}^f, \quad (8)$$

where $E_{2\text{sub}}^f$ is the formation energy of the substitutional pair. The mixing enthalpy is calculated as

$$\Delta H = E_{\text{tot}}(\text{Ni}_x\text{Re}_y) - xE_{\text{tot}}(\text{Ni}) - yE_{\text{tot}}(\text{Re}), \quad (9)$$

where $E_{\text{tot}}(\text{Ni}_x\text{Re}_y)$, $E_{\text{tot}}(\text{Ni})$, and $E_{\text{tot}}(\text{Re})$ are the total energies per atom of Ni_xRe_y , fcc Ni, and hcp Re, respectively.

To calculate the binding energy of substitutional Re in Ni we employ a $4 \times 4 \times 4$ bulk supercell having the equilibrium lattice constant. The properties of Ni_xRe_y calculated by P-MEAM and DFT are listed in table 5. As can be seen the P-MEAM calculated cohesive energy and mixing enthalpy as well as the lattice constant and bulk modulus of NiRe in the CsCl structure are in excellent agreement with DFT. The mixing enthalpy is positive indicating that this phase is unstable at $T = 0 \text{ K}$. Nevertheless, both P-MEAM and DFT calculate negative mixing enthalpy for Ni_4Re in the D1_a structure. In agreement with DFT, the P-MEAM calculated Re substitutional formation energy under Re rich conditions is negative. Due to the large

Table 5. Calculated material properties of Ni–Re binaries. The mixing enthalpy, ΔH_f is in eV/formula unit, cohesive energies, E_c are given in eV/atom and the lattice parameters, a and c , in Å. The elastic constants are in GPa. Substitutional and interstitial formation energies and nearest neighbor substitutional binding energies are in eV. Properties with an asterisk [*] are included in the materials' database (training set). All other quantities were used to evaluate the transferability of the potentials.

	P-MEAM	DFT
CsCl NiRe (1:1)		
(*) E_c	−6.165	−6.14
(*) a	2.95	2.95
(*) B	291	293
B'	5.14	4.78
(*) ΔH_f	0.15	0.67
(*) C_{11}	193	186
(*) C_{12}	342	354
(*) C_{44}	250	144
D1 _a NiRe (4:1)		
E_c	−5.17	−5.73
a	5.53	5.67
c	3.91	3.58
B	243	249
B'	5.08	6.28
ΔH_f	−0.043	−0.29
C_{11}	409	359
C_{12}	147	165
C_{44}	123	161
C_{33}	457	338
C_{13}	154	201
I4/mmm NiRe (3:1)		
E_c	−5.31	−5.73
a	3.64	3.56
c	7.30	7.38
B	273	285
B'	5.21	5.13
ΔH_f	0.14	0.11
C_{11}	363	328
C_{12}	250	248
C_{44}	255	157
C_{33}	401	365
C_{13}	207	192
Cu ₃ Au Ni ₃ Re		
E_c	−5.30	−5.61
a	3.64	3.63
B	274	227
B'	4.94	4.35
ΔH_f	0.17	0.77
C_{11}	395	239
C_{12}	215	196
C_{44}	221	113

(continued on next page)

Table 5. Continued

	P-MEAM	DFT
	NaCl NiRe (1:1)	
E_c	-5.58	-5.32
a	5.01	4.85
B	201	233
B'	5.01	4.72
ΔH_f	1.31	2.33
C_{11}	558	428
C_{12}	22	133
C_{44}	10	-54
$^{(*)}E_{\text{sub}}$	0.03	0.34
$^{(*)}E_{\text{inter/oct}}$	7.22	6.93
E_{binding}	0.05	-0.26

size mismatch between Ni and Re atoms, both P-MEAM and DFT predict positive interstitial formation and substitutional binding energies.

3.2.6. Melting temperatures. Ni based superalloys with Re are used in high temperature applications. Hence, it is of interest to calculate melting temperatures of Ni, Re, and Ni–Re binaries with our potential. The melting temperatures are calculated by employing the moving interface method which eliminates the artifacts of superheating [36]. We employ $200 \times 70 \times 70 \text{ \AA}^3$ orthogonal supercells consisting of $\approx 5 \times 10^4$ atoms. A solid–liquid interface is created normal to the x direction of the supercell by melting half of the crystal under zero pressure while keeping the other half of the crystal to its crystalline state. In the next step, the velocities of all atoms are reassigned to be equivalent to a temperature, T_{guess} , which is an educated guess of the melting temperature, T_m . The system is then equilibrated under zero pressure along the interface normal for a time of 50 ps in the isothermal–isobaric (NPT) ensemble. Next, the barostat is turned off and the system is allowed to evolve for further 20 ps within the canonical (NVT) ensemble. Then, the thermostat is turned off and the calculation continues within the microcanonical (NVE) ensemble for another 20 ps. During the latter period the temperature is monitored. If at the end of the procedure the current temperature is lower (higher) than the actual melting temperature, the interface moves toward the solid (liquid) phase, respectively.

Based on the aforementioned procedure we calculate the melting temperatures for Ni and Re to be equal to $1550 \pm 10 \text{ K}$ and $4350 \pm 20 \text{ K}$, respectively. These values compare well with the experimental values of 1455, 3186 K, respectively [33]. We also calculate the melting temperature of Ni–Re alloys. We consider five different Re concentrations in the range ≈ 2 –14 at%. The Re atoms are randomly distributed in substitutional sites in the Ni host matrix. The melting temperature of the binaries with respect to that of Ni is plotted against the Re content in figure 8.

4. Fracture in Ni and Ni–Re

To investigate fracture in Ni, we evaluate the stress intensity factor by employing LEFM (see section 2). For the $\langle 112 \rangle \{111\}$ slip system, we consider six different crack configurations that vary with respect to the crack propagation direction and the crack plane. In addition, all possible dissociations of the Burgers vector in the Thompson tetrahedron are considered. The angles θ and ϕ between the slip and the crack planes, and between the crack front normal and the

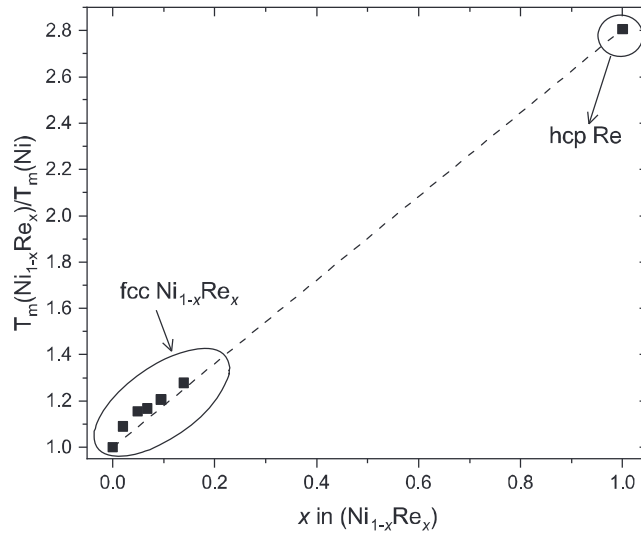


Figure 8. Melting temperature of $\text{Ni}_{1-x}\text{Re}_x$ with respect to the melting temperature of Ni ($T_m(\text{Ni}_{1-x}\text{Re}_x)/T_m(\text{Ni})$) as function of Re content x . For $x = 1$ Re in the hcp structure is considered. For all other contents the fcc structure is considered. The dashed line is a guide to the eye and connects Ni with Re melting temperatures.

Table 6. Critical stress intensity factors K_{Rice} , K_{Griffith} , and K_{CZM} obtained from LEFM using DFT and P-MEAM calculated parameters (see equations (1)–(3)). K_{1c} is obtained from atomistic simulations employing the P-MEAM potential. Six different crack configurations in the $\langle 112 \rangle \{111\}$ slip system are considered. The intensity factors are in $\text{MPa m}^{1/2}$. For each crack configuration the angles θ and ϕ between the slip and the crack plane and between the crack front normal and the Burgers vector are listed. The observed behavior in the atomistic simulations, i.e. brittle vs ductile is given in the last column.

Crack direction/plane	DFT		P-MEAM			Large scale simulations			Observed behavior	
	θ	ϕ	K_{CZM}	K_{Griffith}	K_{Rice}	K_{CZM}	K_{Griffith}	K_{Rice}		K_{1c}
[100]/(010)	54.73	35.26	1.22	1.22	0.97	1.06	1.08	1.06	1.0	Brittle
[1 $\bar{1}$ 0]/(111)	90	19.47	1.14	1.14	0.88	0.96	0.97	0.97	0.90	Brittle
[1 $\bar{1}$ 2]/(1 $\bar{1}$ $\bar{1}$)	61.87	19.47	1.14	1.14	0.82	0.96	0.97	0.91	0.91	Ductile
[1 $\bar{1}$ 0]/(1 $\bar{1}$ $\bar{2}$)	90	0	1.23	1.23	0.84	1.04	1.05	0.93	1.0	Ductile
[010]/(10 $\bar{1}$)	54.73	30	1.25	1.25	0.92	1.06	1.07	1.01	0.9	Ductile
[1 $\bar{1}$ 0]/(001)	90	144.73	1.22	1.22	0.99	1.06	1.08	1.08	1.0	Brittle

Burgers vector (see equation (1)) are calculated using the Thompson tetrahedron. The list of all considered crack configurations are given in table 6.

Next, we introduce an atomically sharp crack in an orthogonal parallelepiped with edge length of about 800 Å along x_1 and x_2 and 10 Å along x_3 (see figure 9). Periodic boundary conditions are applied along x_3 . This simulation box contains more than 4×10^5 atoms. The crack tip is placed at the axes origin with the crack propagation direction along x_1 . The normal to the crack plane is along x_2 . The crack is loaded by imposing the displacement field $\mathbf{u} = (u_1, u_2)$ of mode I fracture under plane-strain conditions within linear elastic fracture

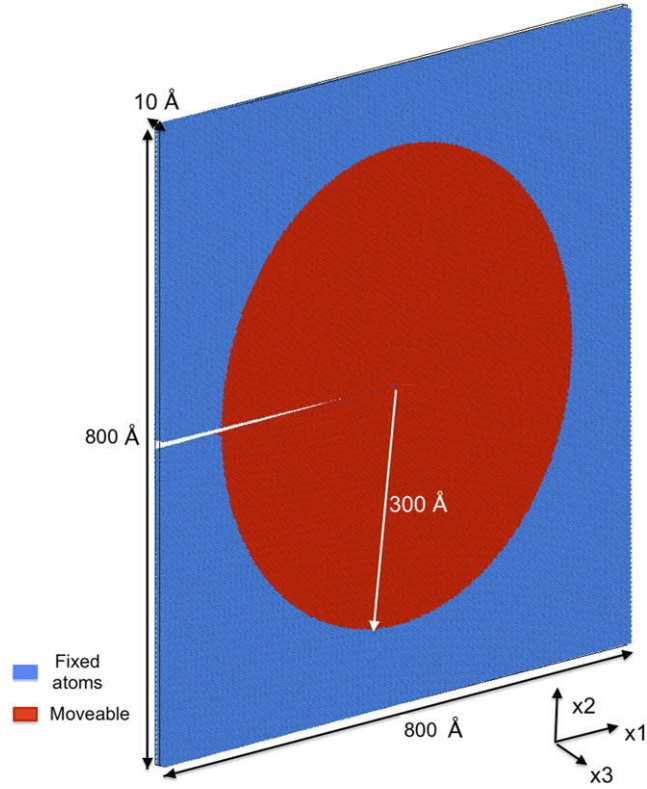


Figure 9. Schematic representation of the simulation box used to model fracture. x_1 is the crack propagation direction, x_2 is the normal to the crack plane, and the crack front is along x_3 . The crack tip is placed at the origin.

theory [9]

$$u_1 = \frac{\Delta K_I}{\mu} \sqrt{\frac{r}{2\pi}} \cos \frac{\beta}{2} \left(1 - 2\nu + \sin^2 \frac{\beta}{2} \right) \quad (10)$$

$$u_2 = \frac{\Delta K_I}{\mu} \sqrt{\frac{r}{2\pi}} \sin \frac{\beta}{2} \left(2 - 2\nu + \cos^2 \frac{\beta}{2} \right), \quad (11)$$

where ΔK_I is the increment in stress intensity factor, and

$$r = \sqrt{x_1^2 + x_2^2} \quad (12)$$

and

$$\beta = \tan^{-1} \left(\frac{x_2}{x_1} \right). \quad (13)$$

The positions of the atoms within a cylinder of radius 300 Å are relaxed until the change in the total energy is less than 10^{-8} eV or the maximum force on the atoms is less than 10^{-12} eV Å⁻¹. The atoms in the outer region are kept fixed. We perform the crack load

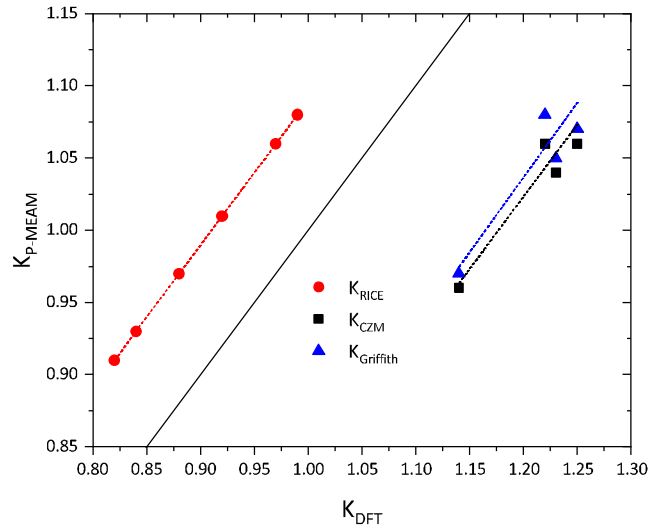


Figure 10. Critical stress intensity factors K_{Rice} , $K_{Griffith}$, and K_{CZM} in MPa $m^{1/2}$ obtained from LEFM and P-MEAM calculated parameters plotted against those obtained from DFT calculated parameters. The solid black line indicates the ideal correlation between P-MEAM and DFT calculated values.

quasistatically, e.g. after atomic relaxation we increase the stress intensity factor by 0.005 MPa $m^{1/2}$ and impose the displacement field on the relaxed structure. This procedure is repeated until the stress intensity factor is 50% higher than the critical stress intensity factor derived by LEFM (see table 6).

Table 6 summarizes the critical stress intensity factors of Ni derived from the four different approaches: atomistic simulations (K_{1c}), cohesive zone model (K_{CZM}), Griffith theory ($K_{Griffith}$) and Rice theory (K_{Rice}). In figure 10 the critical stress intensity factors calculated by LEFM using P-MEAM calculated parameters (see equations (1)–(3)) are plotted against those using DFT calculated parameters. There is an excellent qualitative agreement between P-MEAM and DFT calculations for K_{Rice} and a good agreement for (K_{CZM}) and ($K_{Griffith}$).

To get an on-atomic-scale view of the fracture behavior, let us first focus on the [100]/(010) system. All three analytical models employing P-MEAM calculated parameters predict similar values of K (1.06–1.08), and hence no clear preference of failure behavior: the P-MEAM calculated K_{Rice} (1.06 MPa $m^{1/2}$) is only 2% smaller than the $K_{Griffith}$ (1.08 MPa $m^{1/2}$) and it is equal to the K_{CZM} (1.06 MPa $m^{1/2}$). However, the direct atomistic simulations reveal a value of 1.0 MPa $m^{1/2}$ for the critical stress intensity factor. This small discrepancy is attributed to the fact that tension shear coupling and the surface tension have not been included in the calculation of the USFE. Figure 11(a) demonstrates the σ_{yy} stress around the crack at $K_{1c} = 1$ MPa $m^{1/2}$. The propagation of the crack tip is depicted in figures 11(b) and (c). The advancement of the crack is obtained by cleavage of the crack plane and the absence of any dislocation activity. Furthermore, as can be clearly seen, the crack tip remains sharp. Therefore, the [100]/(010) crack system is brittle.

For both DFT and P-MEAM calculated parameters the [112]/(111) system exhibits the lowest LEFM calculated critical stress intensity factor, i.e. a ductile crack opening behavior is predicted. Indeed, as can be seen in figure 12(a), the crack propagation is accompanied by the nucleation of a Shockley partial dislocation with Burgers vector of type $b = a/6\langle 112 \rangle$. The

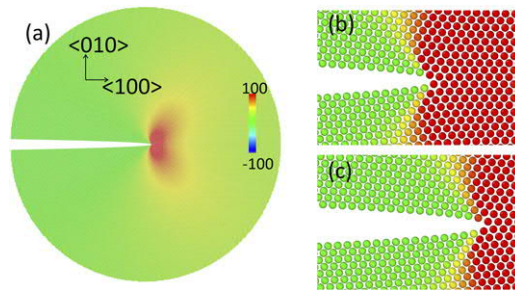


Figure 11. (a) σ_{yy} stress distribution around the $[100]/(010)$ crack tip system at $K_{Ic} = 1$ $\text{MPa m}^{1/2}$. The z -contrast is in GPa. Zoom in of the crack tip region before (b) and after (c) the crack propagation.

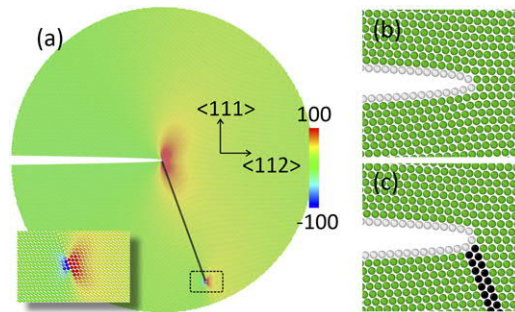


Figure 12. (a) σ_{yy} stress distribution around the $[1\bar{1}2]/(1\bar{1}\bar{1})$ crack tip system at $K_{Ic} = 0.91$ $\text{MPa m}^{1/2}$. The z -contrast is in GPa. The inset in the left-bottom panel is a zoom into the region around the core of the emitted dislocation. It highlights the characteristics of an edge type dislocation, i.e. the tensile (red) and compressive (blue) regions. The black circles denote Ni atoms in the hcp configuration and indicate the stacking fault that is left behind the glide away of the dislocation from the crack tip. (b) and (c) Zoom into the crack tip before and after nucleation and emission of the dislocation, respectively. The green and white disks denote Ni atoms in the fcc bulk-like configuration and at the surface, respectively.

partial glides away from the crack tip and leaves behind a stacking fault. In figures 12(b) and (c) the atomic geometries of the crack tip before and after dislocation nucleation are shown, respectively. As can be seen, the crack opening is accompanied by a blunted crack tip.

The atomic radius of Re is larger than that of Ni. Therefore, Re substitutionals are energetically more favorable in the tensile strained regions of the host matrix, as at the crack tip region for mode I fracture (see figures 11(a) and 12(a)). In order to investigate how solute concentrations of Re affect the critical stress intensity factor, we consider the $[1\bar{1}2]/(1\bar{1}\bar{1})$ crack system. As it has already been mentioned, this system demonstrates the lowest critical stress intensity factor for Ni and hence it constitutes the most suitable system to investigate enhanced ductility due to Re. Re substitutionals are introduced randomly in the Ni host matrix using similar method shown by Zu *et al* [37]. The concentrations of the solutes is varied from 0.5 at.% to 3.5 at.%. For each Re concentration we construct two different samples. The incorporation of Re is

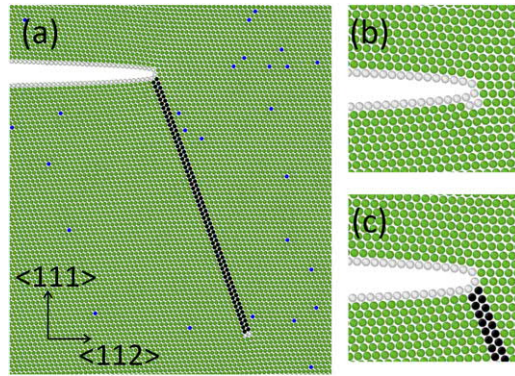


Figure 13. (a) Snapshot extracted from the crack opening simulation of the $[1\bar{1}2]/(1\bar{1}\bar{1})$ system in Ni with 0.6 at.% substitutional Re at $K_{Ic} = 0.87 \text{ MPa m}^{1/2}$. (b) and (c) Zoom-in of the crack tip region at the nucleus of the partial dislocation before and after the dislocation has glided away from the tip, respectively. Green and blue balls represent Ni and Re atoms, respectively. Black balls are atoms in the hcp configuration and white balls are atoms with in a configuration other than fcc, hcp, or bcc and correspond to surface or dislocation core atoms.

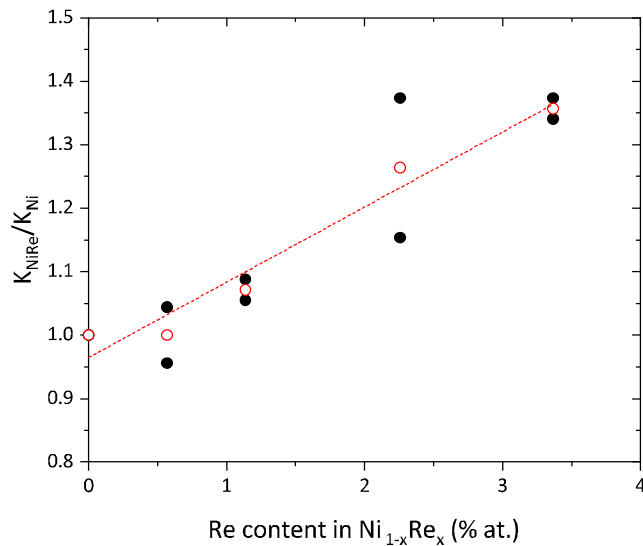


Figure 14. Ratio of critical stress intensity factor of $\text{Ni}_{1-x}\text{Re}_x$ (K_{NiRe}) to that of Ni (K_{Ni}) for different Re contents for mode I fracture in the $[1\bar{1}2]/(1\bar{1}\bar{1})$ crack system. Filled/black dots are values derived from the fracture simulations. Open/red dots are the average values for each Re content. The dashed line is a linear fit to the average values.

followed by a full relaxation of the atomic positions. For the fracture calculations we employ the same methodology as applied for the Ni host matrix.

Our calculations reveal that the addition of substitutional Re does not alter the nature of the crack propagation. For all Re contents considered, the crack growth is associated with nucleation and emission of a dislocation, i.e. the crack opening behavior is ductile. Figures 13(a)–(c)

show a cross sectional view of the crack tip before and after the nucleation and emission of the dislocation for 0.6 at.% Re content. As can be seen, after the dislocation emission the crack tip is blunted and the glide away from the dislocation leaves behind a stacking fault. The critical stress intensity factor as function of the Re content is shown in figure 14. The critical stress intensity factor increases monotonously with the Re content and is $\approx 35\%$ larger than the critical value of Ni for 3.5 at.% Re content. Therefore, with the addition of Re, the stress required to nucleate dislocations becomes higher, hence the value of K increases. The increase of the critical stress intensity factor with the Re content is consistent with existing theoretical [38, 39] work, which further validates the performance and suitability of the here constructed P-MEAM for future studies of Ni–Re alloys.

5. Conclusions

In the present study we have developed 2NN-MEAM potentials for Ni, Re and Ni–Re alloys with a focus on large scale calculations of fracture. To parametrize the potentials, we employed density functional theory calculations and calculated cohesive energies, lattice constants for the ground state and higher energy crystal structures, vacancy formation energies, surface and generalized stacking fault energies, traction separation profiles, cohesive strengths, critical opening displacements, and works of separation. Using these properties and elastic constants we built a materials' database to fit and evaluate the potentials.

A strong emphasis is given on an accurate description of surface energies, generalized stacking fault energies, works of separation, and traction separation profiles, as these properties play a dominant role in fracture. Our potentials provide excellent qualitative and quantitative agreement with DFT calculations of these properties. Furthermore, they successfully overcome the spurious oscillations that show up in the long range tail of traction separation profiles when using the existing interatomic potentials for Ni–Re alloys.

We evaluated the performance of these potentials by employing large scale atomistic calculations of fracture and crack propagation in the $\langle 112 \rangle \{111\}$ fcc slip system. We considered mode I fracture in Ni and NiRe alloy with low Re content. These calculations revealed that the $[1\bar{1}2]/(1\bar{1}\bar{1})$ crack system in Ni has the lowest critical stress intensity factor considering Griffith, Rice and CZM formulations. For this system crack propagation proceeds through nucleation and emission of Shockley partial dislocations, i.e. clearly showing ductile fracture. Alloying with small amounts of Re did not alter the nature of fracture, i.e. it remains ductile, but it increases the critical stress intensity factor. Such trend is in line with the aforementioned *Rhenium effect* [6] and consistent with DFT calculations showing an increase in the intrinsic ductility parameter of Ni due to Re [40]. In summary, the potential constructed in this study is well suited to be employed in large scale fracture simulations of Ni and Ni–Re alloys.

Data availability statement

The data that support the findings of this study are available upon reasonable request from the authors.

Appendix A. Nomenclature

DFT	Density functional theory
EAM	Embedded atom method

2NN-MEAM	Second nearest neighbor modified embedded atom method
LEFM	Linear elastic fracture mechanics
GSFE	Generalized stacking fault energy
CZM	Cohesive zone model
GGA	Generalized gradient approximation
PBE	Perdew–Burke–Ernzerhof
PAW	Projector augmented wave
USFE	Unstable stacking fault energy
fcc	Face centered cubic
hcp	Hexagonal closed pack
bcc	Body centered cubic
sc	Simple cubic

Appendix B. MEAM formalism

A detailed review on MEAM potentials for unary and binary systems can be found in the work of Jelenik *et al* [41]. The modified embedded atom method (MEAM) potentials [42] constitutes an extension of the embedded atom method (EAM) developed by Daw *et al* [43, 44]. In the EAM potentials, the total energy is written as the sum of the short range pair energy and the embedding energy. The latter depends on the electron density which has a spherical symmetry. MEAM potentials further include the angular dependency of the electron density. In MEAM potentials the total energy is written as: [42],

$$E = \sum_i \left[F_i(\bar{\rho}_i) + \frac{1}{2} \sum_{j \neq i} \phi_{ij}(R_{ij}) \right]. \quad (\text{B1})$$

Here, $F_i(\bar{\rho}_i)$ is the embedding energy of atom i , which is a function of the background electron density ($\bar{\rho}_i$) at site i [41, 42]. $\phi(R_{ij})$ is the pair energy and R_{ij} is the interatomic distance between atoms i and j . The embedding energy is defined as the energy required to place an atom at the site i having a background electron density $\bar{\rho}_i$ [41, 42]. This function has the following form

$$F_i(\bar{\rho}_i) = \begin{cases} A_i E_i^0 \bar{\rho}_i \ln(\bar{\rho}_i), & \text{if } \bar{\rho}_i \geq 0 \\ -A_i E_i^0 \bar{\rho}_i, & \text{otherwise} \end{cases} \quad (\text{B2})$$

where E_i^0 is the sublimation energy (negative of the cohesive energy) and A_i is a fitting parameter that depends on the element type of atom i . This can be further considered as equivalent to the Jellium model where the exchange and correlation energy is a functional of the uniform electron gas density in space [43, 44]. The background electron density has the following form

$$\bar{\rho}_i = \frac{\rho_i^{(0)}}{\rho_i^0} G(\Gamma_i) \quad (\text{B3})$$

where,

$$\Gamma_i = \sum_{k=1}^3 t_i^{(k)} \left(\frac{\rho_i^{(k)}}{\rho_i^{(0)}} \right)^2 \quad (\text{B4})$$

and

$$G(\Gamma_i) = \begin{cases} \sqrt{1 + \Gamma_i}, & \text{if } \Gamma_i \geq -1 \\ -\sqrt{|1 + \Gamma_i|}, & \text{if } \Gamma_i < -1 \end{cases}. \quad (\text{B5})$$

The electron densities of different order, i.e. $\rho_i^{(k)}$ can be calculated from equations (B8)–(B12). In equation (B3), ρ_i^0 is the reference electron density and given as

$$\rho_i^0 = \rho_{i0} Z_{i0} G(\Gamma_i^{\text{ref}}), \quad (\text{B6})$$

where ρ_{i0} is an element dependent electron density scaling. Z_{i0} is the first nearest neighbor coordination in the reference structure. For fcc and hcp crystals the nearest neighbor coordination is 12. The functional form for the electron density of the reference structure is given as:

$$\Gamma_i^{\text{ref}} = \frac{1}{Z_{i0}^2} \sum_k^3 t_i^{(k)} s_i^{(k)}. \quad (\text{B7})$$

Here, $s_i^{(k)}$ is a crystal structure dependent shape factor of atom i . The values of the shape factor can be used as described by Baskes *et al* [42]. The partial electron densities in equations (B3)–(B5) are obtained from the superposition of atomic densities scaled by screening function S_{ij} as follows,

$$\rho_i^{(0)} = \sum_{j \neq i} \rho_j^{a(0)}(r_{ij}) S_{ij} \quad (\text{B8})$$

$$(\rho_i^{(1)})^2 = \sum_{\alpha} \left[\sum_{j \neq i} \rho_j^{a(1)} \frac{r_{ij\alpha}}{r_{ij}} S_{ij} \right]^2 \quad (\text{B9})$$

$$(\rho_i^{(2)})^2 = \sum_{\alpha, \beta} \left[\sum_{j \neq i} \rho_j^{a(2)} \frac{r_{ij\alpha} r_{ij\beta}}{r_{ij}^2} S_{ij} \right]^2 - \frac{1}{3} \left[\sum_{j \neq i} \rho_j^{a(2)}(r_{ij}) S_{ij} \right]^2 \quad (\text{B10})$$

$$(\rho_i^{(3)})^2 = \sum_{\alpha, \beta, \gamma} \left[\sum_{j \neq i} \rho_j^{a(3)} \frac{r_{ij\alpha} r_{ij\beta} r_{ij\gamma}}{r_{ij}^3} S_{ij} \right]^2 - \quad (\text{B11})$$

$$\frac{3}{5} \sum_{\alpha} \left[\sum_{j \neq i} \rho_j^{a(3)}(r_{ij\alpha}) S_{ij} \right]^2. \quad (\text{B12})$$

Here $r_{ij\alpha}$ is the α th component of the displacement vector. S_{ij} is the screening function between atoms i and j and it is discussed in the following section. Equations (B8)–(B12) are background electron densities including higher order terms. In the EAM potentials a linear superposition of spherical average electron densities is used [42]. In the MEAM formalism also higher order terms are included. The way the background electron densities are constructed in equations (B8)–(B12), can be thought as s , p , d , and f electron densities [42]. In

equations (B8)–(B12), the unscreened electron density, $\rho_i^{a(k)}$ is given as an exponential decay function:

$$\rho_i^{a(k)}(r_{ij}) = \rho_{i0} \exp \left[-\beta_i^k \left(\frac{r_{ij}}{r_{ij}^0} - 1 \right) \right]. \quad (\text{B13})$$

Here, r_{ij}^0 is the nearest neighbor distance in the reference structure and $\beta^{(k)}$ is obtained during fitting. The weighting factor for the electron density can be given as:

$$t_i^{(k)} = \frac{\sum_{j \neq i} t_{0,j}^k \rho_j^{a(0)} S_{ij}}{\sum_{j \neq i} (t_{0,j}^k)^2 \rho_j^{a(0)} S_{ij}}. \quad (\text{B14})$$

The atomic interactions are screened with the same formalism as the electron density. The atomic interactions are screened via introducing a screening function in the pair energy term:

$$\phi_{ij}(r_{ij}) = \bar{\phi}_{ij}(r_{ij}) S_{ij}, \quad (\text{B15})$$

where $\bar{\phi}_{ij}(r_{ij})$ has the following form,

$$\bar{\phi}_{ij}(r_{ij}) = \frac{1}{Z_{ij}} \left[2E_{ij}^u - F_i \left(\frac{Z_{ij}}{Z_i} \rho_j^{a(0)}(r_{ij}) \right) - F_j \left(\frac{Z_{ij}}{Z_j} \rho_i^{a(0)}(r_{ij}) \right) \right]. \quad (\text{B16})$$

The energy term $E_{ij}^u(r_{ij})$ is taken from the Rose universal equation of state where the binding energy is represented via an exponential decay function [45]:

$$E_{ij}^u(r_{ij}) = -E_{ij}(1 + a_{ij}^*(r_{ij}))e^{-a_{ij}^*(r_{ij})}, \quad (\text{B17})$$

where a_{ij}^* is the interatomic distance scaled with respect to the equilibrium lattice spacing. This parameter is calculated from the following equation:

$$a_{ij}^* = \alpha \left(\frac{r_{ij}}{r_{ij}^0} - 1 \right). \quad (\text{B18})$$

α is a dimensionless parameter and is related to bulk modulus, cohesive energy and equilibrium lattice volume in the following way [46]

$$\alpha = \sqrt{\frac{9B\Omega}{E_c}}. \quad (\text{B19})$$

One of the main differences of the MEAM potentials with respect to other valence force fields is the use of many body screening. Many body screening in MEAM potentials describes how interactions between two atoms are screened by neighboring atoms. Let us first consider the functional form of screening function S_{ij} between atom i and j . In the MEAM formalism, the total screening function is written as a product of a radial cutoff function and a three body term:

$$S_{ij} = \bar{S}_{ij} f_c \left(\frac{r_c - r_{ij}}{\Delta r} \right). \quad (\text{B20})$$

The smooth cut off function f_c is defined as:

$$f_c(x) = \begin{cases} 1 & \text{if } x \geq 1 \\ -[1 - (1 - x)^4]^2, & \text{if } 0 \geq x \leq 1 \\ 0 & \text{if } x \leq 0 \end{cases} \quad (\text{B21})$$

and the three body terms are obtained by summing up the function as following,

$$\bar{S}_{ij} = \prod_{k \neq i, j} S_{ikj} \quad (\text{B22})$$

with

$$S_{ikj} = f_c \left(\frac{C_{ikj} - C_{\min, ikj}}{C_{\max, ikj} - C_{\min, ikj}} \right). \quad (\text{B23})$$

The functional form of C_{ikj} is,

$$C_{ikj} = \frac{2(X_{ij} + X_{jk}) - (X_{ij} - X_{jk})^2 - 1}{1 - (X_{ij} - X_{jk})^2}, \quad (\text{B24})$$

where $X_{ik} = (R_{ik}/R_{ij})^2$ and $X_{kj} = (R_{kj}/R_{ij})^2$. C_{\min} and C_{\max} are the limiting values of C .

In order to provide an intuitive picture of screening in MEAM potentials one can consider a series of ellipses passing

$$X^2 + \frac{Y^2}{C} = \frac{1}{4}. \quad (\text{B25})$$

The major axis of the ellipse is along the y direction and the minor x is the line segment connecting atoms i and k . If atom j lies outside the ellipse defined by $C = C_{\max}$ then it does not screen the interaction between i and k , i.e. $S_{ijk} = 1.0$. However, if atom j lies inside the ellipse defined by $C = C_{\min}$ then it completely screens the interaction between i and k and $S_{ijk} = 0.0$. In all other cases, atom j partially screens the aforementioned interaction and S_{ijk} scales between 0 and 1.

Once the interatomic potentials of the individual elements are ready, the binary interatomic potentials are constructed using the individual element parameters as well as newly parametrized parameters. In a binary system, the total energy per atoms $E_{ij}^u(R)$ is written as


$$E_{ij}^u(R) = \frac{1}{2} \left[F_i(\bar{\rho}_i) + F_j(\bar{\rho}_j) + Z_1^{ij} \phi_{ij}(R) + \frac{1}{2} Z_2^{ij} S_i \phi_{ii}(aR) + S_j \phi_{jj}(aR) \right]. \quad (\text{B26})$$

Here R is the nearest neighbor distance in the binary system. F_i and F_j are the embedding energy term for individual elements, Z_1^{ij} and Z_2^{ij} are the coordinations of first and second nearest neighbors and a is the ratio of second and first nearest neighbor distances. The pair interaction between the different types of atoms is calculated as:

$$\phi_{ij}(R) = \frac{1}{Z_1^{ij}} \left[2E_{ij}^u(R) - F_i(\bar{\rho}_i) - F_j(\bar{\rho}_j) - \frac{1}{2} Z_2^{ij} S_i \phi_{ii}(aR) + S_j \phi_{jj}(aR) \right] \quad (\text{B27})$$

ORCID iDs

Masud Alam  <https://orcid.org/0000-0002-6634-5365>

Liverios Lymperakis  <https://orcid.org/0000-0002-4883-3728>

Sébastien Groh  <https://orcid.org/0000-0003-0022-7048>

References

- [1] Caron P and Khan T 1999 *Aerosp. Sci. Technol.* **3** 513
- [2] Caron P 2000 *Superalloys* **2000** 737
- [3] Pollock T M 1995 *Simul. Mater. Sci. Eng.* **B 32** 255
- [4] Giamei A F and Anton D L 1985 *Metall. Trans. A* **16** 1997
- [5] Wu X et al 2020 *Nat. Commun.* **11** 389
- [6] Huang M and Zhu J 2016 *Rare Met.* **35** 127
- [7] Maisel S B, Schindzielorz N, Mottura A, Reed R C and Müller S 2014 *Phys. Rev. B* **90** 094110
- [8] Andric P and Curtin W A 2017 *J. Mech. Phys. Solids* **106** 315
- [9] Andric P and Curtin W A 2018 *Modelling Simul. Mater. Sci. Eng.* **27** 013001
- [10] Wu Z and Curtin W A 2015 *Acta Mater.* **88** 1
- [11] Abraham F F, Walkup R, Gao H, Duchaineau M, De La Rubia T D and Seager M 2002 *Proc. Natl Acad. Sci.* **99** 5777
- [12] Groh S and Alam M 2015 *Modelling Simul. Mater. Sci. Eng.* **23** 045008
- [13] Wu Z, Francis M F and Curtin W A 2015 *Modelling Simul. Mater. Sci. Eng.* **23** 015004
- [14] Lee B-J, Shim J-H and Baskes M I 2003 *Phys. Rev. B* **68** 144112
- [15] Ko W-S, Grabowski B and Neugebauer J 2015 *Phys. Rev. B* **92** 134107
- [16] Etesami S A and Asadi E 2018 *J. Phys. Chem. Solids* **112** 61
- [17] Mishin Y, Farkas D, Mehl M J and Papaconstantopoulos D A 1999 *Phys. Rev. B* **59** 3393
- [18] Bonny G, Bakaev A, Terentyev D and Mastrokov Y A 2017 *J. Appl. Phys.* **121** 165107
- [19] Baskes M I and Johnson R A 1994 *Modelling Simul. Mater. Sci. Eng.* **2** 147
- [20] Ko W-S and Lee B-J 2014 *Phil. Mag.* **94** 1745
- [21] Griffith A A 1921 *Phil. Trans. R. Soc. A* **221** 163
- [22] Rice J R 1992 *J. Mech. Phys. Solids* **40** 239
- [23] Vitek V 1968 *Phil. Mag.* **18** 773
- [24] Cleveringa H H M, Van der Giessen E and Needleman A 2000 *J. Mech. Phys. Solids* **48** 1133
- [25] Groh S, Olarnrithinun S, Curtin W A, Needleman A, Deshpande V S and Van der Giessen E 2008 *Phil. Mag.* **88** 3565
- [26] Möller J J, Bitzek E, Janisch R, ul Hassan H and Hartmaier A 2018 *J. Mater. Res.* **33** 3750
- [27] Kresse G and Furthmüller J 1996 *Phys. Rev. B* **54** 169
- [28] Alam M, Lymperakis L and Neugebauer J 2020 *Phys. Rev. Mater.* **4** 083604
- [29] Beckstein O, Klepeis J E, Hart G L W and Pankratov O 2001 *Phys. Rev. B* **63** 134112
- [30] Alam M and Groh S 2015 *J. Phys. Chem. Solids* **82** 1
- [31] Liebscher C H et al 2018 *Phys. Rev. Lett.* **121** 015702
- [32] Vitos L, Ruban A V, Skriver H L and Kollár J 1998 *Surf. Sci.* **411** 186
- [33] Okamoto H 2012 *J. Phase Equilib. Diffus.* **33** 346
- [34] Kittel C, McEuen P and McEuen P 1996 *Introduction to Solid State Physics* vol 8 (New York: Wiley)
- [35] de Jong M, Olmsted D L, van de Walle A and Asta M 2012 *Phys. Rev. B* **86** 224101
- [36] Morris J R, Wang C Z, Ho K M and Chan C T 1994 *Phys. Rev. B* **49** 3109
- [37] Zu G and Groh S 2016 *Theor. Appl. Fract. Mech.* **85** 236
- [38] Liu Z-G, Wang C-Y and Yu T 2013 *Modelling Simul. Mater. Sci. Eng.* **21** 045009
- [39] Liu Z-G, Wang C-Y and Yu T 2015 *Comput. Mater. Sci.* **97** 127
- [40] Breidi A, Fries S G, Palumbo M and Ruban A V 2016 *Comput. Mater. Sci.* **117** 45
- [41] Jelinek B, Groh S, Horstemeyer M F, Houze J, Kim S G, Wagner G J, Moitra A and Baskes M I 2012 *Phys. Rev. B* **85** 245102

- [42] Baskes M I 1992 *Phys. Rev. B* **46** 2727
- [43] Daw M S and Baskes M I 1983 *Phys. Rev. Lett.* **50** 1285
- [44] Daw M S and Baskes M I 1984 *Phys. Rev. B* **29** 6443
- [45] Rose J H, Smith J R, Guinea F and Ferrante J 1984 *Phys. Rev. B* **29** 2963
- [46] Baskes M I 1992 *Phys. Rev. B* **46** 2727